



RESEARCH ARTICLE

10.1002/2017JC013119

Key Points:

- Sea ice deformation localizes along lines in high-resolution viscous-plastic sea ice models
- The model reproduces spatial scaling properties also observed in satellite data
- The model underestimates temporal scaling compared to satellite data

Supporting Information:

- Supporting Information S1

Correspondence to:

N. Hutter,
nils.hutter@awi.de

Citation:

Hutter, N., Losch, M., & Menemenlis, D. (2018). Scaling properties of arctic sea ice deformation in a high-resolution viscous-plastic sea ice model and in satellite observations. *Journal of Geophysical Research: Oceans*, 123. <https://doi.org/10.1002/2017JC013119>

Received 22 MAY 2017

Accepted 1 JAN 2018

Accepted article online 8 JAN 2018

© 2018. The Authors.

This is an open access article under the terms of the Creative Commons Attribution-NonCommercial-NoDerivs License, which permits use and distribution in any medium, provided the original work is properly cited, the use is non-commercial and no modifications or adaptations are made.

Scaling Properties of Arctic Sea Ice Deformation in a High-Resolution Viscous-Plastic Sea Ice Model and in Satellite Observations

Nils Hutter¹ , Martin Losch¹ , and Dimitris Menemenlis²

¹Alfred-Wegener-Institute für Polar-und Meeresforschung, Bremerhaven, Germany, ²Jet Propulsion Laboratory, California Institute of Technology, Pasadena, California, USA

Abstract Sea ice models with the traditional viscous-plastic (VP) rheology and very small horizontal grid spacing can resolve leads and deformation rates localized along Linear Kinematic Features (LKF). In a 1 km pan-Arctic sea ice-ocean simulation, the small-scale sea ice deformations are evaluated with a scaling analysis in relation to satellite observations of the Envisat Geophysical Processor System (EGPS) in the Central Arctic. A new coupled scaling analysis for data on Eulerian grids is used to determine the spatial and temporal scaling and the coupling between temporal and spatial scales. The spatial scaling of the modeled sea ice deformation implies multifractality. It is also coupled to temporal scales and varies realistically by region and season. The agreement of the spatial scaling with satellite observations challenges previous results with VP models at coarser resolution, which did not reproduce the observed scaling. The temporal scaling analysis shows that the VP model, as configured in this 1 km simulation, does not fully resolve the intermittency of sea ice deformation that is observed in satellite data.

1. Introduction

Oriented fractures scatter Arctic sea ice in all seasons. They divide the ice cover into many ice floes and narrow lineaments of open water (Kwok, 2001; Marko & Thomson, 1977; Richter-Menge et al., 2002). The fragmentation of ice is caused by stress resulting from surface wind associated with weather systems, ocean eddies, geometric boundaries such as the coastline or a fast ice edge (Richter-Menge et al., 2002), tides (Holloway & Proshutinsky, 2007), ocean waves (Squire et al., 1995), or swell originating from Arctic storms (Asplin et al., 2012). Convergent motion in the ice pack forms pressure ridges whereas stripes of open ocean, so-called leads, develop during divergent motion. These narrow and long structures are often referred to as Linear Kinematic Features (LKF) due to their formation by the kinematic processes: opening, closing, and shear (Kwok, 2001).

Systems of leads in Arctic sea ice are observed across all scales from aerial photographs to satellite images—pointing to self-similar properties (or a fractal structure) of sea ice. This impression is supported by the floe size distribution following a power-law scaling (Rothrock & Thorndike, 1984). Power-law scaling was also observed in lead width distributions (Lindsay & Rothrock, 1995), in fracture and faulting of sea ice (Weiss, 2003), and in sea ice deformation (Marsan et al., 2004; Rampal et al., 2008; Stern & Lindsay, 2009).

The mean total deformation $\dot{\epsilon}_t$ at the spatial scale L was found to follow a power-law

$$\langle \dot{\epsilon}_t^q(L) \rangle \sim L^{-\beta(q)}, \tag{1}$$

with a scaling exponent $\beta(q)$, which is a quadratic function of the order of moment q ranging from 0.5 to 3 (Marsan et al., 2004). The quadratic shape of $\beta(q)$ suggests multifractal characteristics of sea ice deformation (Marsan et al., 2004). Typical values for the first-order moment scaling coefficient around $\beta(1) \sim 0.2$ for deformation rates were derived from satellite data (Girard et al., 2009; Marsan et al., 2004; Stern & Lindsay, 2009) and from buoy data (Hutchings et al., 2011) in winter time. The spatial scaling exponent follows a seasonal cycle mainly driven by the varying ice strength. It increases during summertime as a result of weaker summer ice being more prone to local deformation (Stern & Lindsay, 2009).

In addition to spatial scaling properties, temporal scaling properties, and a coupling between temporal and spatial scaling exponents were found for sea ice deformation derived from the dispersion of buoys:

$$\langle \dot{\epsilon}_d(L, \tau) \rangle \sim L^{-\beta(\tau)} \sim \tau^{-\alpha(L)}, \quad (2)$$

where the temporal scaling exponent $\alpha(L)$ depends on the spatial scale L and the spatial scaling exponent $\beta(\tau)$ on the temporal scale τ (Marsan & Weiss, 2010; Oikkonen et al., 2017; Rampal et al., 2008). A review on scaling properties of sea ice deformation can be found in Weiss and Dansereau (2017).

Scaling analyses are a useful tool for evaluating small-scale sea ice deformation produced by sea ice models (Bouillon & Rampal, 2015a; Girard et al., 2009; Rampal et al., 2016) because they quantify the strong localization of deformation in space (heterogeneity) and in time (intermittency), which can then be compared to the observed localization in satellite (Herman & Glowacki, 2012; Marsan et al., 2004; Stern & Lindsay, 2009) and buoy data (Hutchings et al., 2011, 2012; Oikkonen et al., 2017; Rampal et al., 2008). The scaling characteristics and multifractality of deformation rates in a VP model with 12 km horizontal grid spacing have been found to significantly disagree with the scaling laws that were estimated from satellite data and buoy trajectories (Girard et al., 2009), even though VP models can realistically represent the large-scale sea ice drift velocity fields (Kwok et al., 2008; Lindsay et al., 2003). Girard et al. (2009) attributed this disagreement to the fact that the extreme localization of large deformation rate events, such as structural failure on subgrid scale, is not properly represented by the VP rheology.

Girard et al. (2011) introduced the elasto-brittle (EB) rheology, previously used in rock mechanics simulations, in order to improve the physical representation of the brittle behavior of sea ice by including a sub-grid scale damage parameter and elastic interaction in a sea ice models. The EB-rheology reproduces the strong localization in space (heterogeneity) (Girard et al., 2011) and in time (intermittency) (Rampal et al., 2016). It has been shown to be practical in a dynamical and thermodynamical sea ice model (Rampal et al., 2016) and, especially with the extension to the Maxwell elasto-brittle rheology (Dansereau et al., 2016), this rheology has the potential to improve the modeling of LKFs in coupled climate models.

Independently of these improvements in sea ice rheology, horizontal grid spacing of climate models is decreasing toward scales that start to resolve large leads. In fact, VP sea ice model solutions show linear failure lines for a grid spacing smaller than ~ 5 km (e.g., Figure 2 in Losch et al. (2014)). Further, Wang et al. (2016) compared different satellite products with sea ice model solutions obtained with an elastic-viscous-plastic (EVP) rheology solver at 4.5 km grid spacing and at first glance found agreement in the regional and seasonal variation of the lead area fraction. There is, however, no thorough evaluation of the spatial and temporal scaling properties at high resolution that would test the characteristic spatial heterogeneity and intermittency of small-scale sea ice deformation in these models.

In this paper, we use model results of a sea ice ocean model with an average grid spacing below 1 km in the Arctic to study the effect of resolved leads on the scaling properties of sea ice deformation in the VP model. To this end, we implement a scaling analysis, which is a combination of a spatial (Marsan et al., 2004) and a temporal scaling analysis (Hutchings et al., 2011; Rampal et al., 2008) for gridded Eulerian data. In doing so, the spatial and temporal scaling characteristics are computed simultaneously and the coupling between both is determined. For evaluation, we use the ENVISAT Geophysical Processor System (EGPS) data set. Furthermore, we examine the seasonal and regional variability of spatial scaling properties and how they depend on the ice condition, that is, sea ice concentration and thickness.

2. Model and Observations

2.1. EGPS Data Set

We use high resolution sea ice drift data from the Envisat Geophysical Processor System (EGPS) for evaluation of the model results. The data are available at <http://rkwok.jpl.nasa.gov/envisat/index.html>. EGPS is the successor of the RADARSAT Geophysical Processor System (RGPS) but it covers different regions (Central Arctic, Canadian Arctic Archipelago, and Ross Sea in Antarctica) and the temporal sampling rate is 1 day, instead of 3 days for RGPS. In contrast to RGPS, the EGPS is not provided as an Arctic wide composite but as single drift data sets. Each drift data set is derived from two overlapping SAR images and is provided on a regular grid with 10 km grid spacing. Note that the widely used RGPS data set has a larger spatial coverage, but is not available for the simulation period.

We compile one sea ice drift and deformation composite from all individual drift data sets in the Central Arctic (see Figure 1) during the period between September 2011 and April 2012. We use the original EGPS

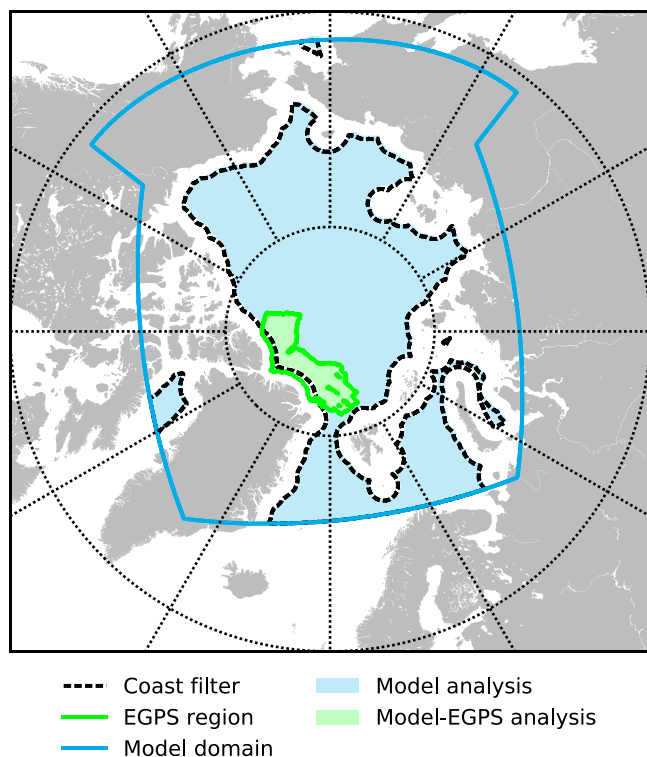


Figure 1. Model domain, region of EGPS data, and the coastline filter. The analysis regions are shaded (blue for model-only analysis and green for model-observation comparison).

grid with a temporal and spatial sampling of 1 day and 10 km on a Polar stereographic projection with a reference latitude of 70°N . For each composite day, all data sets that overlap at least in part with the given day of the composite are identified. Strain rates are computed from velocities by finite difference for all those drift data sets and averaged with a weight corresponding to the size of the temporal overlap with the composite day. Because the EGPS data are provided on a regular grid with constant grid spacing within the polar stereographic projection, metric effects can be neglected in the computation of the velocity gradients. The start time and the time span of individual drift data sets can vary, so that one data set can contribute to more than 1 day in the obtained composite. Similarly, the drift data within 1 day composite is not necessarily recorded at exact the same time, which leads to slight differences in the mean drift within the velocity fields of the composite.

2.2. Model Description

The simulation we analyze is one of a series of so-called global Latitude-Longitude-polar-Cap (LLC; Forget et al., 2015) simulations carried out with the Massachusetts Institute of Technology general circulation model (MITgcm, Marshall et al., 1997; MITgcm Group, 2017). A $\frac{1}{12}^{\circ}$ LLC simulation is initialized on 1 January 2010 from a data constrained $\frac{1}{6}^{\circ}$ simulation provided by the Estimating the Circulation and Climate of the Ocean, Phase II (ECCO2) project (Menemenlis et al., 2008). The $\frac{1}{12}^{\circ}$ simulation is integrated for 1 year with ERA-Interim (Dee et al., 2011) surface boundary conditions. On 1 January 2011, surface boundary conditions are switched to the 0.14° ECMWF atmospheric operational model analysis starting in 2011 (European Centre

for Medium-Range Weather Forecasts, 2011). All atmospheric fields are provided at 6 hourly intervals and converted to surface fluxes using bulk formulae (Large & Yeager, 2004) and a dynamic-thermodynamic sea ice model (Losch et al., 2010). Starting on 1 January 2011, surface boundary conditions also include tidal forcing for the 16 most significant components, applied as additional atmospheric pressure forcing as in Ponte et al. (2015). A $\frac{1}{24}^{\circ}$ LLC simulation is initialized on 17 January 2011 from the $\frac{1}{12}^{\circ}$ simulation and a $\frac{1}{48}^{\circ}$ LLC simulation is initialized on 10 September 2011 from the $\frac{1}{24}^{\circ}$ simulation. In this study, we use model output from the $\frac{1}{48}^{\circ}$ LLC simulation, hereinafter labeled as LLC4320, where 4320 refers to the dimension of the polar cap. The LLC4320 simulation is integrated with 25 s time step and prognostic model variables are saved at hourly intervals. At the time of this study, output was available for the period 13 September 2011 to 8 October 2012.

Published model-data comparisons for the LLC4320 simulation to date are limited to a Drake Passage study (Rocha et al., 2016a), which compared along-track wavenumber spectra of kinetic energy to Acoustic Doppler Current Profiler data, and a Kuroshio Extension study (Rocha et al., 2016b), which established that the upper ocean stratification and variability in that region is well captured by the LLC4320 simulation. This study is the first to examine the LLC4320 model output in the Arctic Ocean, where horizontal grid spacing is a little below 1 km. Bathymetry is from the International Bathymetric Chart of the Arctic Ocean (IBCAO) Version 2.23 (Jakobsson et al., 2008). The sea ice model uses both dynamics and thermodynamics (Losch et al., 2010). Ocean and sea ice parameterizations and parameters are from Nguyen et al. (2011) with the following modifications: (1) the salt-plume parameterization of Nguyen et al. (2009) is turned off; (2) the nonlocal transport term in the K-Profile Parameterization (KPP) of Large et al. (1994) is turned off; (3) barotropic time stepping uses Crank-Nicolson instead of Adams-Bashforth; (4) no slip condition is applied at lateral boundary conditions; (5) lead closing parameter H_0 is 0.05 m instead of 0.61 m; and (6) sea ice strength P^* is 27.5 kN m^{-1} instead of 22.6 kN m^{-1} . Note that the LLC4320 model parameters have not yet been optimized in any way to fit observations; the above changes relative to Nguyen et al. (2011) were primarily applied in order to make the LLC4320 integration numerically stable.

None of the above changes relative to Nguyen et al. (2011) are essential to the sea ice model except for H_0 and P^* . A larger P^* makes the ice “stiffer,” but the value of 27.5 kN m^{-1} is well within the accepted range, in fact, it is the value suggested by Hibler (1979). The lead closing parameter H_0 determines the thickness of newly formed ice (Hibler, 1979) and is a very powerful tuning parameter. The very small value used here implies very thin new ice of 0.05 m, so that a partially sea ice free grid cell in freezing conditions can be covered by thin ice very quickly, reducing further heat flux and hence further ice growth. Essentially, low H_0 lead to overall thinner ice. The increased resolution and addition of tidal forcing in the LLC4320 simulation relative to Nguyen et al. (2011) caused excessively thick sea ice to form with $H_0=0.61 \text{ m}$, especially in shallow coastal regions, causing the LLC4320 simulation to go unstable. We reduced H_0 to 0.05 m to keep sea ice thinner. Although this lower value of H_0 allowed the integration to remain stable, it is almost certainly not the optimal value for this parameter.

2.3. Processing of Modeled Velocity Fields

For the comparison of model results and EGPS data, we sample the model fields in the same way as the EGPS data: a set of virtual buoys is initialized each day on the grid covered by the EGPS composite; for each model output step (i.e., every 1 h) streamlines through the virtual buoys are computed assuming a stationary velocity field within this time step, and the buoys are advected along the streamlines (Blanke & Raynaud, 1997); the virtual buoys are reinitialized every 24 h on the EGPS grid; velocity gradients and deformation rates are calculated from the drift of the virtual buoys by finite differences. Both EGPS data and the sampled LLC4320 model data set agree exactly in the regional coverage and the observation period (13 September 2011 to 8 April 2012). The integration of daily trajectories emulates the EGPS sampling procedure of determining sea ice drift by tracking single points in the ice. In both cases, the EGPS and the retrieved LLC4320 composite, the final product is sea ice drift and deformation on an Eulerian grid.

3. Methods

3.1. Scaling Analysis

Except for Herman and Glowacki (2012), who used gridded Eulerian data in a spatial scaling analysis, scaling analyses of sea ice deformation are based on Lagrangian trajectories, either derived from satellite images (Marsan et al., 2004; Stern & Lindsay, 2009), recorded by buoys (Hutchings et al., 2011, 2012; Rampal et al., 2008), or modeled in a Lagrangian framework (Rampal et al., 2016). Both Lagrangian and Eulerian approach should, in theory, lead to the same spatial scaling results (if small timescales are considered where the advection of ice between two time steps is negligible), but the temporal scaling properties depend on the deformation history of individual ice flows. Eulerian averaging over a fixed box in space neglects the advection of this deformation history, so that this memory effect can only be taken into account by following one parcel of ice over time. Hence, the temporal scaling analysis requires a Lagrangian approach. However, the computation of strain rates from Lagrangian trajectories is known to introduce errors by the choice of cell boundaries and the discontinuities in ice motion (Lindsay & Stern, 2003). These errors lead to an overestimation of the scaling exponents (Bouillon & Rampal, 2015b). Because both the LLC output and the EGPS data set are provided on Eulerian grids, the integration of trajectories from the gridded fields will introduce errors for each position on the trajectory. This position error is especially pronounced for the EGPS data, because the single data sets of the composite are recorded during different time periods leading to differences in the mean drift in the composite (see supporting information Figure S1). These differences in mean drift will result in spurious deformation lines along the boundaries of single data sets. The model fields do not include these artificial velocity gradients because all velocities are computed in the same time interval, so that a Lagrangian approach will generate differences in the scaling analysis between observations and model that are not in the data but derive only from the analysis method.

We developed a method that combines both the Lagrangian tracking of ice and the computation of deformation rates on the original Eulerian grid. In doing so, trajectories of virtual buoys starting at the vertices of averaging boxes are integrated. The partial velocity derivatives computed on the Eulerian grid via finite differences are averaged in the advected boxes. After computing the deformation rates from the averaged velocity derivatives, this Lagrangian Sampling of Eulerian gridded data (LSE) provides a data set that combines the benefit of Eulerian gridded velocity data to precisely determine the deformation rates and the necessity of tracking the ice motion for temporal scaling. Figure 2 illustrates the three different methods.

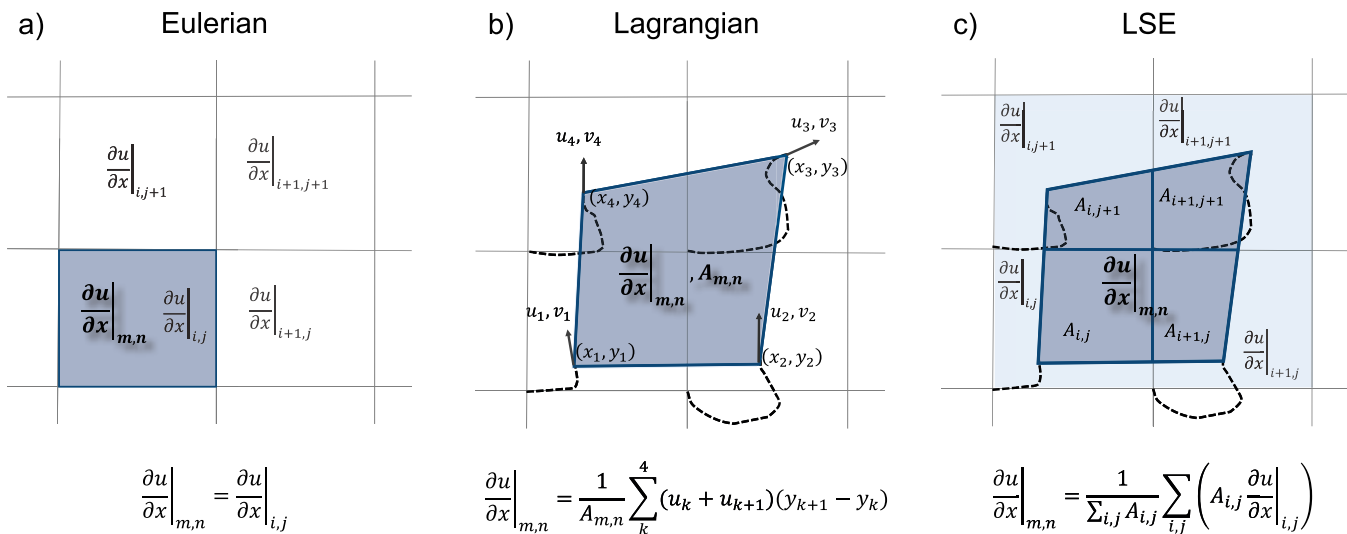


Figure 2. Overview of the three different methods of determining the velocity gradient in the scaling analysis. (a) In an Eulerian representation each box coincides with a grid box and the velocity gradient is computed by finite differences from the Eulerian gridded velocity data. The Lagrangian and LSE method use trajectories integrated from the velocity data that are given as dashed lines to define the displaced boxes. (b) In the Lagrangian method, the velocities at the vertices of a displaced box are reconstructed from the trajectories and the gradient is determined by a line integral over the boundary of box (shaded in dark blue). (c) For the LSE method the gradients computed on the Eulerian grid are averaged over all grid cells that overlap with the averaging box (shaded in pale blue) weighted by the area of overlap (shaded in dark blue).

The virtual buoys defining the LSE averaging boxes are initialized on the corner points of the Eulerian grid of the EGPS composite. Because the EGPS data is provided as a set of drift vectors, we compute the trajectory by interpolating the drift vector at the position of the trajectory for each time step and by advecting the position accordingly. The model trajectories are computed in the same way using the retrieved LLC data to minimize sampling uncertainties. All virtual buoy positions that are closer than 150 km to the coast, or lie in regions with sea ice concentration lower than 0.15 are removed from the data, because we are only interested in the deformation of the dense ice pack. For each time step, the position of each drifted averaging box in the Eulerian grid is determined. The partial velocity derivatives of all Eulerian grid cells that overlap partly or fully with the LSE averaging box are averaged weighted by the overlapping area (see Figure 2). As we use the corner points of the EGPS grid and four vertices per box, all LSE averaging boxes coincide with one EGPS grid cell at time zero. In the following time steps, the network of averaging boxes will constantly drift and deform. The final output of the LSE method is a data set of velocity gradients at the spatial scale of the EGPS grid of $L=10$ km and a temporal resolution of $\tau=1$ day that follows the ice parcels that are enclosed by the averaging boxes. The computation of deformation rates at larger spatial and temporal scales is then performed by the following scaling analysis.

To account for the coupling between temporal and spatial scales, we developed a method that simultaneously computes temporal and spatial scaling characteristics. To this end, a temporal component is added to the spatial scaling analysis of Marsan et al. (2004). In Marsan et al. (2004) strain rates are averaged in squares of size $L^* \times L^*$, to obtain strain rates at the spatial scale L . Please note that there is a difference between the nominal spatial scale L^* determining the size of the box and the effective spatial scale L associated with the box, as the box may not be entirely filled with data points due to filtering and data coverage.

Prior to the spatial averaging we average the strain rates of each LSE box over the temporal scale τ^* . Strongly deformed LSE boxes are filtered by removing boxes that (1) are smaller than half the area of the initial EGPS cells $A_i < 0.5A_{org}$, (2) are larger than twice the area of the initial EGPS cells $A_i > 2A_{org}$, or (3) no longer form a quadrilateral box. The time covered by all unfiltered points is given by $T=N\Delta t$, where N is the number of unfiltered data points and Δt is the temporal resolution of the data. After averaging, all grid points are removed, for which the time T is below the threshold $T < 0.5\tau^*$. In the next step, we compute the mean of all remaining temporally averaged strain rates inside the $L^* \times L^*$ box. We define the $L^* \times L^*$ boxes in the first time step as a set of $\frac{L^*}{\Delta x} \times \frac{L^*}{\Delta x}$ neighboring LSE boxes, where Δx defines the EGPS grid

resolution. The position and shape of the averaging boxes will change with time as the defining LSE boxes will be advected and deformed by the ice motion.

Again due to filtering, the $L^* \times L^*$ box may not be completely filled with valid data. If the area with valid data falls below the threshold $\sqrt{\sum A_i} < 0.5 L^*$, the average strain rate of this box is removed. The effective scales associated with the average strain rate of the cuboid are given by the coverage of the data after filtering, that is, for the effective temporal scale $\tau = T$ and for the effective spatial scale $L = \sqrt{\sum A_i}$.

The sampling of deformation rates following the ice motion is only necessary for scaling analyses that include temporal averaging of deformation. Whenever spatial scaling at the initial temporal scale of the drift data is computed, the tracking of single ice parcels is not necessary, and we can compute spatial averages on the Eulerian grid as done in Herman and Glowacki (2012). The second part of this paper evaluates only the spatial scaling properties of the LLC model results and all analyses will be performed on the Eulerian grid to reduce computational costs.

3.2. Evaluation of the Analysis Method

To evaluate the new scaling analysis for gridded Eulerian data, we quantify the sensitivity of the scaling properties to the method of computing spatial gradients. This information helps to assess our results and to compare them to previous results that were obtained by Lagrangian and Eulerian methods. To this end, we integrate trajectories of virtual buoys initialized on the EGPS grid using the EGPS drift data as described above. Every 7 days, a new set of virtual buoys is initialized for the time period from 1 January 2012 to 31 March 2012. The drift of each set of virtual buoys is computed for 14 day intervals. We perform the above introduced scaling analysis with (1) strain rates that are averaged using the LSE method and (2) strain rates that are computed from the trajectories using line integrals (Lindsay & Stern, 2003). In addition, we compute spatial scaling at the initial temporal scale of $\tau = 1$ day using strain rates computed on the Eulerian grid (Figure 3).

As expected (Bouillon & Rampal, 2015b; Lindsay & Stern, 2003), the mean deformation rate computed from the Lagrangian trajectories is larger than the one computed on the Eulerian grid for all analyzed spatial scales. The lower mean deformation rates of LSE compared to the ones computed on the Eulerian grid are also plausible, because the partial velocity derivatives computed by LSE are averages of the Eulerian partial velocity derivatives and thereby smaller.

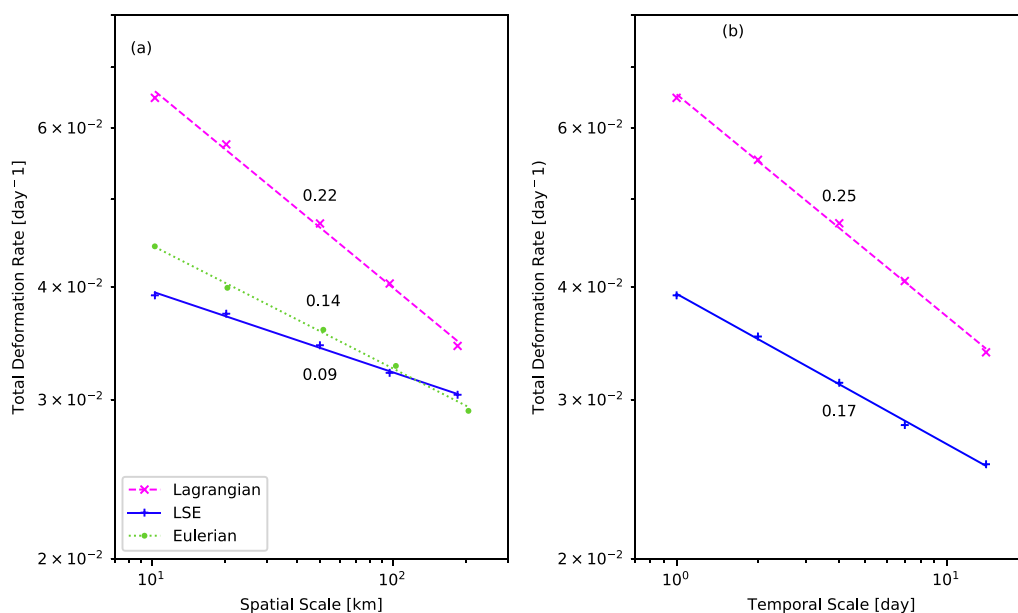


Figure 3. Scaling analyses for three different ways to compute strain rates that are LES, line integrals on trajectories (Lagrangian), and finite differences on Eulerian grid (Eulerian). (a) Spatial scaling analysis of Arctic sea ice deformation for the month January, February, and March 2012 at a temporal scale of 1 day computed from the EGPS composite. (b) Temporal scaling analysis of Arctic sea ice deformation for the month January, February, and March 2012 at a spatial scale of 10 km computed from the EGPS composite.

All three approaches lead to a power-law scaling of sea ice deformation with regard to spatial and temporal scales. The higher spatial scaling exponents of the Lagrangian approach compared to the Eulerian approach can be explained by the overestimation of deformation rates due to the use of line integrals, and by the spurious shear lines due to the integration of composite velocity fields. Bouillon and Rampal (2015b) found that the Lagrangian method may overestimate the spatial scaling coefficient by up to 60%; we observe 57%. Due to the reduction of mean deformation rates, the spatial scaling exponent determined with LSE underestimates the Eulerian scaling exponent by 55%. The temporal scaling exponents of LSE underestimate the exponents of the Lagrangian analysis by 47%.

With this we can relate the scaling exponents of the LSE analysis to the results of other RGPS and buoy studies performed on a Lagrangian and an Eulerian grid. Although the underestimation of scaling exponents of LSE compared to the Lagrangian method complicates the comparison to previous results, we believe it is the appropriate method to analyze the Eulerian data in this study, because it avoids spurious overestimation of deformation rates and reduces the effect of varying mean drift within one time step of the EGPS composite.

4. Results

At first glance, the very high-resolution VP simulation is very different from model results with coarser resolution: the deformation rates ((b) divergence and (c) shear in Figure 4) concentrate along failure lines in the ice pack. These failure lines are characterized by low sea ice concentration (Figure 4a). We do not observe smooth variations of deformation rates over large areas as presented in Girard et al. (2009). In addition, the Probability Density Functions (PDF) of simulated deformation rates show power-law tails (see supporting information Figure S3). Compared to results of VP models with 4.5 km resolution (Losch et al., 2014; Spreen et al., 2016), there is a clear increase in the amount of detail with resolution.

4.1. Model-Observation Comparison

In the first part of our analysis, we compare the model results directly to the EGPS data set. The comparison is confined to the region where the EGPS data set provides drift data for at least 14 consecutive days, that is, the Central Arctic North of Greenland (green-shaded area in Figure 1). In analogy to other scaling comparisons between model and observations (Girard et al., 2009; Rampal et al., 2016), our scaling analysis is limited to the winter months January, February, and March when the Arctic is fully ice covered with a dense ice pack. For April and May, satellite data are not available. We use the LSE scaling analysis on virtual buoy trajectories for this comparison, which are initialized every 7 days on the EGPS grid and last 14 days.

Broadly speaking, model results and observations agree on the order of magnitude of the deformation, but the observed deformation rates are slightly higher (Figure 5). The spatial scaling exponent of the EGPS data ranges from 0.09 ($\tau=1$ day) to 0.06 ($\tau=14$ days). For the same temporal scales, the scaling exponents of the model data are around 0.06 and show no clear dependence on the temporal scale. Although the model

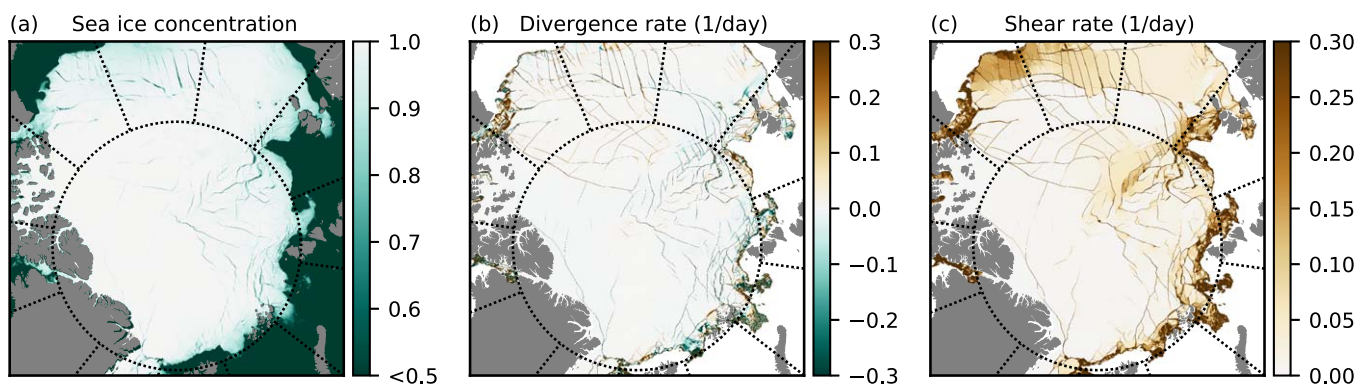


Figure 4. (a) Sea ice concentration, (b) divergence rate, and (c) shear rate of the LLC4320 run for 21 September 2011, 2 pm. The deformation rates concentrate along the leads seen in the sea ice concentration and mark Linear Kinematic Features (LKF).

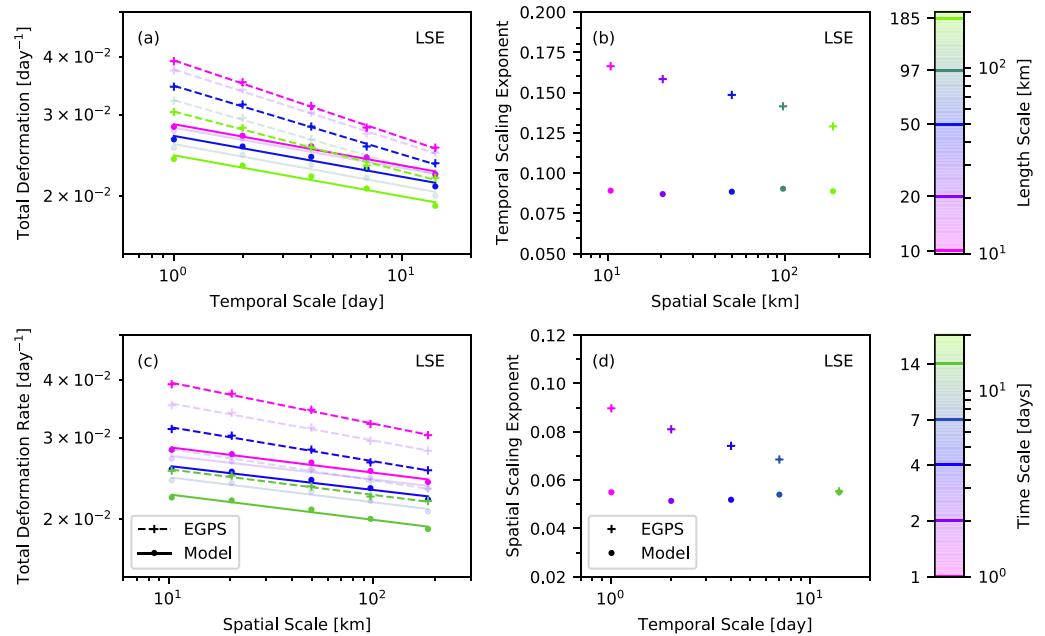


Figure 5. Spatial-temporal scaling properties of model output compared to EGPS data. The comparison is confined to the area of the EGPS composite for each day and to the period of 1 January 2012 to 31 March 2012.

reproduces the spatial scaling characteristics observed from EGPS for large temporal scales, there is no coupling of spatial and temporal scales in the modeled sea ice deformation.

With the power-law scaling of the moments (equation (1)), we assess the multifractal characteristics of the modeled and observed sea ice deformation. For the temporal scale of $\tau=1$ day, moments of the order $q=0.5, 1, 1.5, 2, 2.5,$ and 3 are computed (Figure 6). The structure function $\beta(q)$ is determined by a power-law

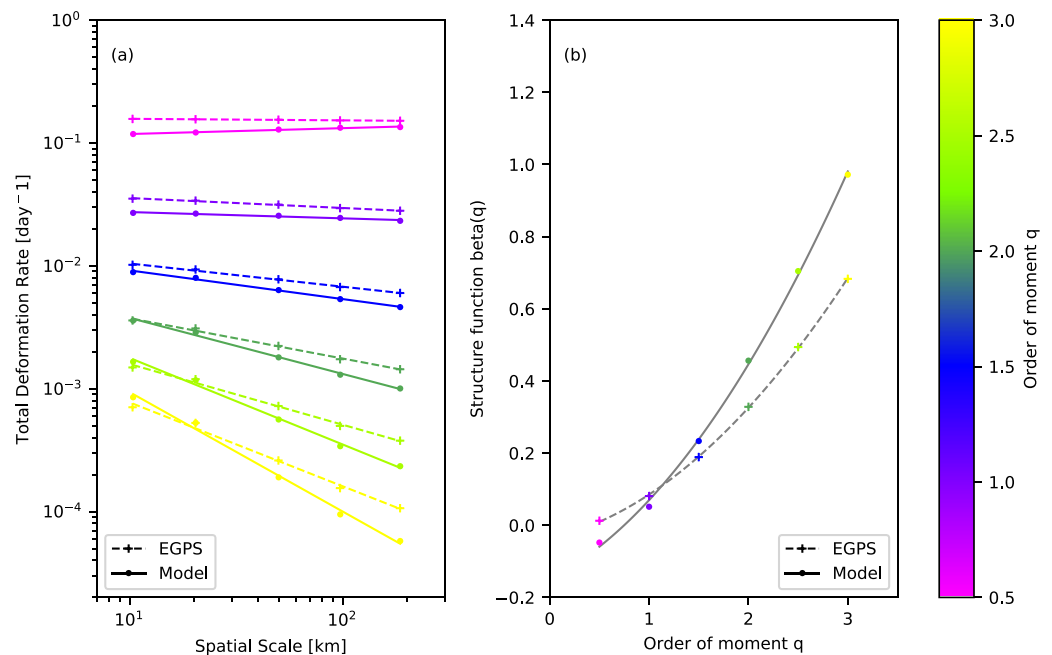


Figure 6. Left plot (a): Spatial scaling analysis for different moments $|e_t^q| \sim L^{-\beta(q)}$ for model output and EGPS data. Right plot (b): Structure function $\beta(q)$ computed from linear fits to left plot. The fit to a quadratic function is given in dashed (EGPS) and solid (model) lines. Comparison is limited to the area of the EGPS data set.

fit to each moment. The structure function is quadratic $\beta(q)=aq^2+bq+c$ with a positive curvature of $a = 0.06$ for the satellite observations and $a = 0.08$ for the model, so that $\beta(q)$ is convex, indicating multifractal characteristics for both data sets.

The good agreement of the spatial scaling characteristics between model and satellite data does not carry over to the Eulerian temporal scaling: for the EGPS data, the temporal scaling exponents range from 0.17 ($L=10$ km) to 0.13 ($L=185$ km), but the temporal scaling exponents of the model are lower with 0.9 (for both $L=10$ km and $L=185$ km) and again show no dependence on the spatial scale (Figure 5). The low scaling exponents imply that the model does not fully represent the intermittent character of sea ice deformation. This corresponds to our observation that leads develop slowly in the model in contrast to spontaneous failure observed from satellite, and once formed persist too long in the ice cover (see supporting information Figure S6). We note, however, that the comparison is limited to one winter and a small region North of Greenland. This region contains fast ice at the coast and high drift velocity in the export regions through Fram Strait and the comparison may be biased by the representation of these very specific sea ice states in the model.

4.2. Pan-Arctic Scaling Properties

After showing that the model at least in part reproduces the scaling characteristics observed in the EGPS data, we extend the spatiotemporal scaling analysis to the entire LLC4320 simulation. The entire model domain (blue-shaded area in Figure 1) and all seasons are taken into account to study the influence of different ice conditions and the seasonal cycle of sea ice deformation. In addition, the model-only analysis includes scales as small as $L = 1$ km and $\tau = 1$ h.

A spatiotemporal scaling analysis tests the effect of reproduced leads on the scaling characteristics of sea ice deformation. We apply the LSE method described in section 3.1 to all data between 1 December 2011 and 30 April 2012 in the entire model domain. To define the LSE boxes, we integrate trajectories of virtual

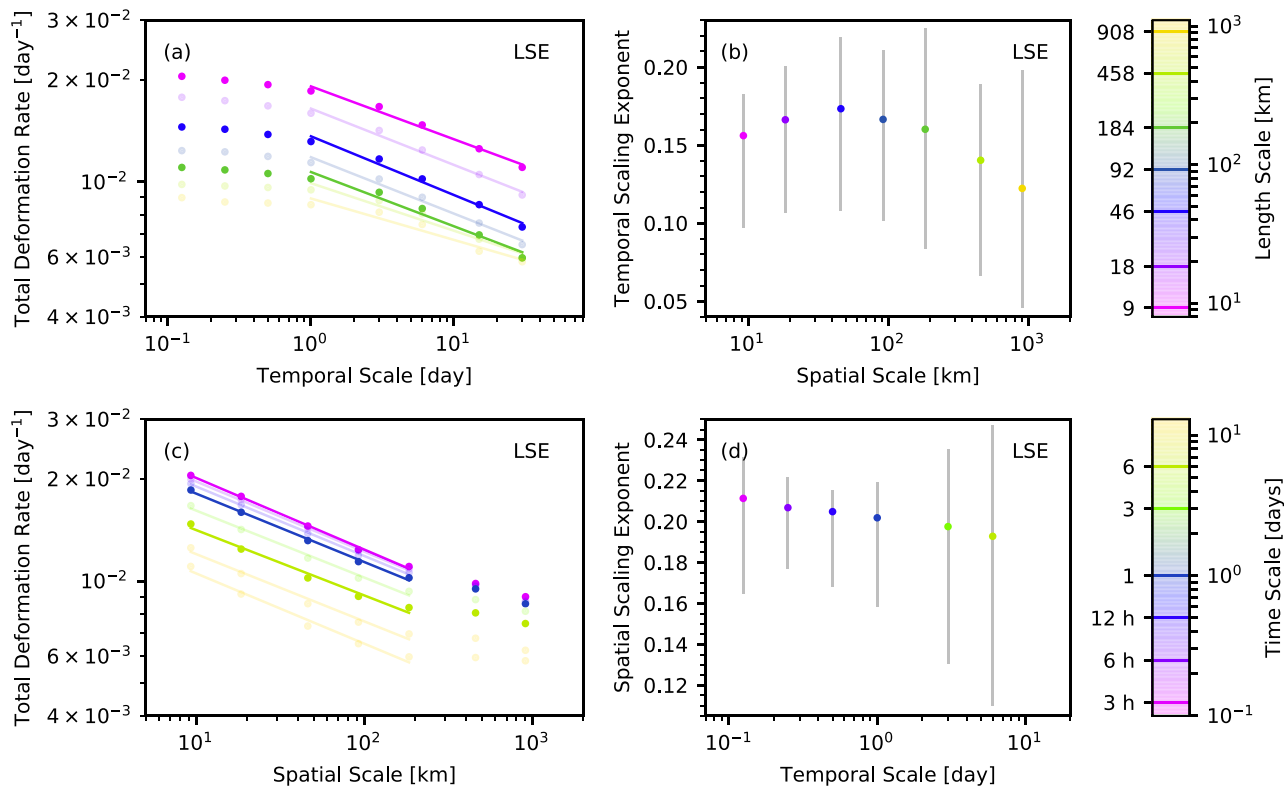


Figure 7. Spatiotemporal scaling of total deformation of the model output in the period between December and April 2012. Total deformation for different spatial and temporal scales is indicated by dots. Power-law fits to this data are presented as lines in the left plots (a) and (c). The right plots (b) and (d) show the power-law exponents of the fit with respect to the spatial scale and the temporal scale, respectively. The error bounds of the scaling exponents are determined by the minimum and maximum slope between successive points of the power-law fit.

buoys that are initialized every 30 days on the model grid with a separation of roughly 10 km. The deformation rates averaged by LSE are computed on the model grid with a horizontal grid spacing of 1 km and a temporal resolution of 1 h.

Figure 7 shows the results of this scaling analysis with the mean deformation at different spatial and temporal scales as well as the induced scaling exponents α and β .

The spatial scaling exponent β ranges from 0.21 ($\tau=3$ h) to 0.19 ($\tau=6$ days). Between this range, it varies approximately linearly with temporal scale. This shows that deformation is strongly localized for small temporal scales, whereas for larger temporal scales the averaging over different deformation events leads to a less heterogeneous deformation field.

The least square fit to the power laws of equation (2) in the temporal scaling analysis (Figure 7a) is restricted to scales larger than $\tau \geq 1$ day. For smaller temporal scales, the power-law flattens, which might be an imprint of the temporal resolution of the wind forcing of 6 h. The flattening of the power-law is also reflected in the uncertainties of the scaling exponents in Figure 7b. Less flattening would lead to smaller uncertainties in the fitted exponents. The temporal scaling exponent does depend linearly on the spatial scale, as it increases from 0.16 at 10 km to the maximum 0.17 at 46 km and decreases again to 0.12 at 908 km.

4.3. Seasonal Variation of Spatial Scaling

In the following three subsections, we restrict the discussion to spatial scaling properties at a temporal scale of $\tau=1$ h. Since no temporal scaling analysis is used in this section and only the initial time step is used, temporal averaging considering the advection of ice is not necessary. Therefore, we use deformation rates computed on the Eulerian model grid for the analysis within this section instead of LSE. We examine the seasonal cycle, the regional variation, and the dependence on the ice condition in analogy to Stern and Lindsay (2009).

For this purpose, we analyze the entire LLC4320 simulation period (13 September 2011 to 8 October 2012). The Arctic model domain is subdivided in boxes of size 500 km \times 500 km with an overlap of 250 km. Within each box with an ice coverage of at least 25%, a spatial scaling analysis is performed for the temporal scale of 1 h.

A clear seasonal cycle is seen in time series of both parameters of the power-law fit, that is, the scaling exponent and the mean deformation at 1 km (Figure 8): while ice is freezing and the ice cover increases, the scaling exponent decreases to a minimum in April. With the onset of the melting season in May, the deformation and its heterogeneity (scaling exponent) increases to a maximum in August.

The seasonality of the deformation parameters is linked to the varying extent of the ice cover, as indicated by the apparent anticorrelation ($R=-0.92$) with the mean sea ice concentration in the model domain (Figure 8). This covariation reflects the coupling of ice strength with concentration (in the model, strength is proportional to $\exp[-C^*(1-A)]$). A closed ice cover at high concentration can, due to its high ice strength, support internal stress propagation over large distances. This "far field effect" leads to smaller differences of the deformation rates across the scales (Stern & Lindsay, 2009). In contrast, stress cannot be redistributed in the loosely packed summer ice, and the number of deformation events increases leading to a very heterogeneous deformation field. In addition to the ice strength, two other factors, namely (1) the effect of the coastline as a boundary for an ice-filled Arctic and (2) the reduced atmospheric momentum transfer due to more stable atmospheric conditions in winter, contribute to the seasonal cycle (Kwok, 2006).

On top of the seasonal cycle, short-term variations with a period of about 2 weeks are observed. We attribute those fluctuations to various weather systems passing the Arctic and initiating sea ice

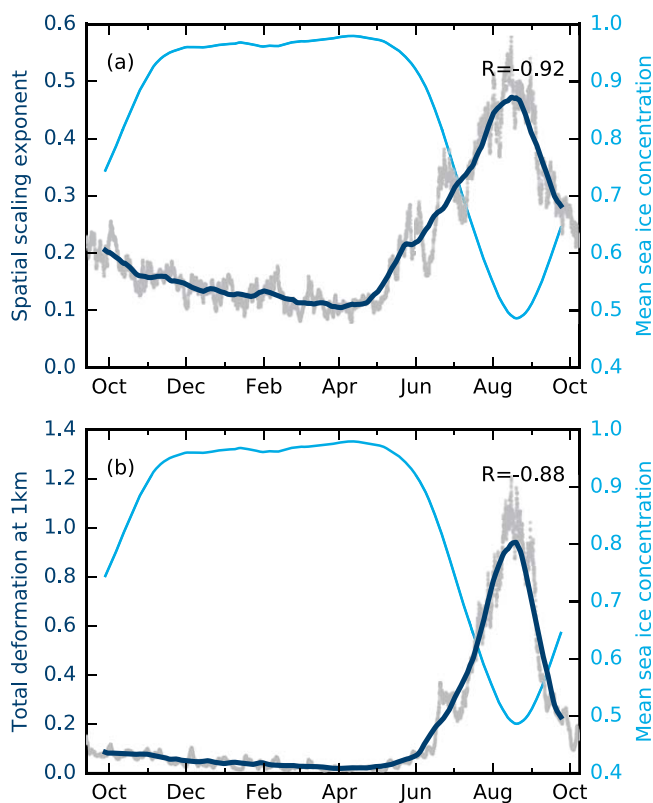


Figure 8. Seasonal variability of the power-law parameters (a) spatial scaling exponent and (b) total deformation at 1 km scale) derived from the model output. In addition, the mean sea ice concentration averaged over all Arctic grid cells is given. The curve represents a running mean with a window size of 1 month.

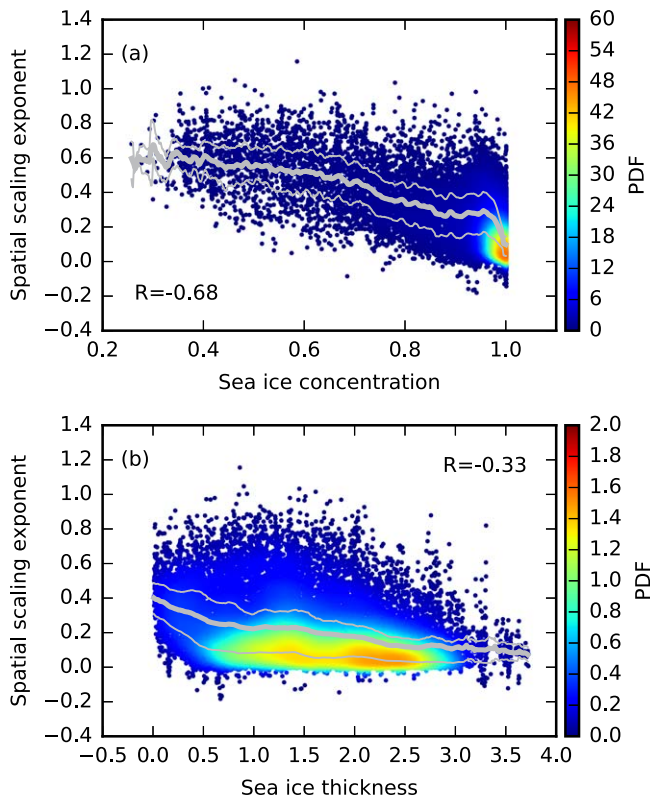


Figure 9. Spatial scaling coefficient as function of (a) sea ice concentration and (b) thickness. The thick gray line shows the running mean with an averaging window of 1% for sea ice concentration and 20 cm for sea ice thickness. The thin lines show the 25th and 75th percentile. Each dot represents the coefficient of an individual grid box. The color indicates their probability density and illustrates the variance of the results (for clarity only 2% of the data are shown for the density).

The higher correlation coefficient between scaling exponent and concentration ($R = -0.68$) compared to thickness ($R = -0.33$) can also be explained by the functional form of the ice strength: ice strength varies exponentially with concentration, but only linearly with thickness. The difference between the correlation coefficients computed for the mean concentration of single boxes (Figure 9) and of the entire Arctic (Figure 8) shows that, in addition to the influence of ice strength, there is an effect of lateral (land) boundaries in an ice-filled Arctic (Kwok, 2006).

4.5. Regional Variation of Spatial Scaling

The regional variation of the scaling exponent in January 2012 is shown in Figure 10. The Central Arctic is mainly characterized by very low scaling exponents ($0 < \beta < 0.09$) because the ice strength is high (high concentration and thickness). At the coast of Alaska toward the Bering Strait, the scaling exponents increase ($0.13 < \beta < 0.21$). The relatively thin ice in this region is prone to deformation leading to very heterogeneous deformation fields. The highest values are found in the Fram Strait and the Barent Sea, where scaling exponents range between 0.17 and 0.5. In those regions opening toward the Atlantic Ocean, the thin and mostly seasonal ice is continuously deformed because of high sea ice velocity shear due to the high ice speed.

5. Discussion

Before putting our results into perspective, we note once again that the LLC4320 simulation has not been adjusted or data constrained in any way. We therefore expect differences between observations and simulation not only for the chaotic components of the circulation, for example, the location of mesoscale eddies or of cracks in the ice, but also for larger-scale properties such as sea ice concentration, thickness, and drift.

deformation. Herman and Glowacki (2012) showed this short-term variability to be driven by synoptic variability for RGPS data.

4.4. Scaling and Ice State

In a classical VP model, the ice strength $P = P^* h \exp[-C^*(1-A)]$ is defined by the ice condition and the two parameters P^* and C^* (Hibler, 1979); in our case, these parameters are $P^* = 27.5 \text{ kN m}^{-2}$ and $C^* = 20$. To examine the influence of ice strength on the spatial scaling exponent and test for different scaling behavior in multiyear and first-year ice, we study its dependence on sea ice concentration A and thickness h . Figure 9 shows the mean sea ice concentration and thickness within each $500 \text{ km} \times 500 \text{ km}$ box (as defined in section 4.3) and its corresponding scaling exponent as a scatter plot, along with the mean scaling exponent given at a certain concentration or thickness.

The lowest mean spatial scaling exponents are found for fully covered boxes. Most points range around a sea ice concentration of one and a scaling exponent of 0.08. For lower sea ice concentrations, the spatial scaling exponent increases strongly and levels off toward very low concentrations, as expected from the exponential form of the strength expression.

The mean spatial scaling exponent also decreases almost linearly with increasing sea ice thickness from 0.4 for very thin ice down to 0.1 for ice thicker than 2 m. The impact of ice thickness, however, is smaller than that of concentration and approximately linear. The variance of the spatial scaling coefficient at a given thickness is higher than the variance at a given concentration, as indicated by the wider spread of spatial scaling exponents in Figure 9, bottom plot.

The trend in both curves is consistent with the ice strength parameterization, showing that the model reproduces the influence of the ice strength on the spatial scaling properties. The influence on the second scaling parameter (mean deformation at 1 km) is similar (not shown).

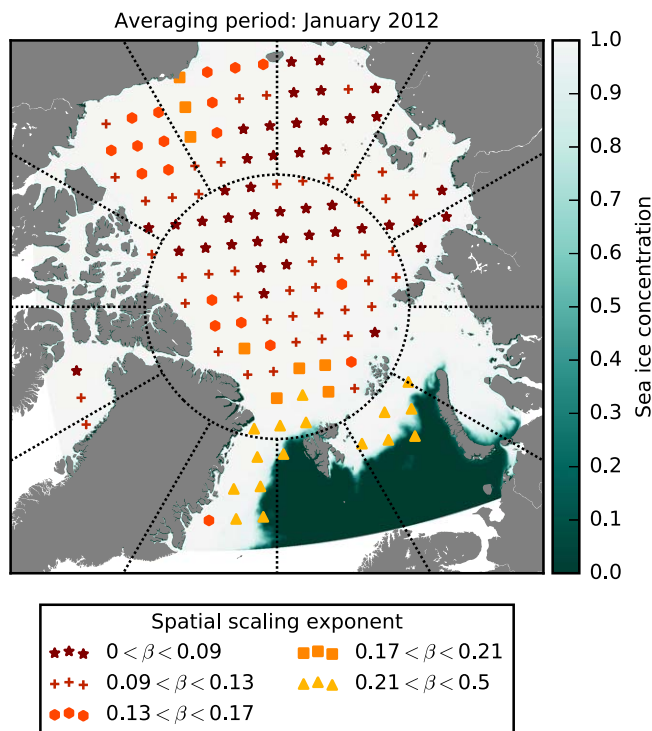


Figure 10. Regional variation of spatial scaling exponent for January 2012. The spatial scaling exponent is given by different markers and the color shading shows the mean sea ice concentration.

The above limitations need to be kept in mind when using the LLC4320 simulation to explore the behavior of VP rheology at high spatial resolution.

The direct comparison of the model results to satellite observations is restricted to the region North of Greenland during the winter months of January, February, and March due to limited satellite data availability. Due to the small area of satellite data, the comparison could also be dominated by local effects. Because of this data limitation, the separate analysis of the model results also needs to be taken into account when evaluating the ability of the model to reproduce scaling characteristics of sea ice deformation. The differences between spatial scaling exponents for the model output and satellite data range from 0.03 at a temporal scale of $\tau=1$ day to perfect agreement at $\tau=14$ days, due to the missing coupling between spatial and temporal scaling.

The spatial scaling exponents derived from the EGPS data set ($\beta(\tau=4 \text{ days})=0.08$) agree well with published numbers for the RGPS data set ($\beta(\tau=3 \text{ days})=0.20$; Marsan et al., 2004; Stern & Lindsay, 2009) considering the underestimation of the used LSE method compared to Lagrangian based referenced studies. Recall that in section 3.2 the Lagrangian scaling analysis for the EGPS data set yielded spatial scaling exponents of 0.22 for the 1 day temporal scale. We observe a dependence of the spatial scaling exponents on the temporal scale in line with previous results (Marsan & Weiss, 2010; Rampal et al., 2008) for satellite observations. In contrast, the model results do not show such a clear coupling in this region. Only in the Pan-Arctic scaling

analysis for the model results, a coupling between spatial scaling exponents and temporal scale is seen, although the coupling is weaker than for satellite observations (variation of 0.02 over a range of two orders magnitudes for the model results in contrast to a variation of 0.03 over one order of magnitude). The space-time coupling exists, because deformation on a short timescale is likely to take place nearby as a reaction to previous deformation (Weiss, 2017), so that averaging deformation over short time periods leads to a strong localization of deformation rates around a few deformation events. Therefore, the weaker coupling in the model points to the model lacking a mechanism that links previous and current deformation. This aspect will be discussed in further detail in the discussion on the temporal scaling at the end of this section.

The spatial scaling for all moments of the modeled deformation rates agrees with the satellite data. The curvature of the structure function of the model ($a = 0.08$) and the satellite data ($a = 0.06$) are slightly lower than previously reported ($a = 0.13$) (Marsan et al., 2004; Rampal et al., 2016), which can be explained using LSE instead of a pure Lagrangian scaling analysis. In summary, the good agreement of the spatial scaling of the model with satellite observations shows that the VP model can reproduce deformation rates that are strongly localized in space, but we observe only a weak coupling to the temporal scale.

The sea ice deformation of the entire model domain is characterized by spatial power-scaling with $\beta=0.20$ for a temporal scale of 3 days compared to RGPS-data-based estimates of $\beta \approx 0.2$ for a timescale of 3 days without filtering (Girard et al., 2009; Hutchings et al., 2011; Marsan et al., 2004; Stern & Lindsay, 2009). Rampal et al. (2016) found the scaling exponent of filtered RGPS data to be $\beta=0.16$ for the shear rate. Taking into account the smoothing by LSE method, the model overestimates the localization of deformation. The smoothing effect of the LSE method may explain part of the underestimation by the model in the restricted region of the model-observation comparison.

We find that the model reproduces the seasonal cycle of scaling coefficients observed by Stern and Lindsay (2009). The strong increase in the scaling exponent in May and the drop to a quasi-steady state in November are captured by the model. A comparison for the short summer period is not possible due to the summer gap of RGPS. However, a maximum at the end of August is plausible considering the minimum sea ice extent at this time.

We find that the seasonal cycle of the scaling coefficients is most likely determined by the ice condition and the ice coverage of the Arctic. The scaling coefficients depend on the ice condition through the ice strength parameterization. Stern and Lindsay (2009) evaluated the dependence of the scaling exponent on the multi-year ice fraction and found lower exponents for more multiyear ice. Comparing this trend to our thickness dependence, the model seems to underestimate deformation rates for thin (presumably first-year) ice, which implies that changing to a higher-order ice strength parameterization, for example $P \sim h^2$ (Rothrock, 1975), might improve the results. We did not analyze the influence of a more stable atmosphere in winter-time on the seasonal cycle, which is the third effect identified by Kwok (2006), but idealized model experiments (not shown here) show a high sensitivity to changes in the wind forcing indicating that this effect should be resolved in the simulation.

The regional distribution of scaling exponents shows that sea ice deformation localizes strongly in less confined regions of high velocities and thin ice, where the velocity gradients are largest and the low ice strength quickly leads to plastic deformation of the ice cover. Stern and Lindsay (2009) also observed the highest exponents in first-year ice at the coast of Alaska and North of the Lincoln Sea. The model underestimates the scaling in regions of first-year ice (coast of Alaska and Siberia), which could be addressed with an adapted ice strength parameterization (see previous paragraph).

For temporal scaling exponents, the differences between model and satellite data are larger. North of Greenland there is no coupling of the temporal scaling exponent to spatial scales in the model. In contrast, the temporal scaling exponents of the Pan-Arctic analysis show a dependence on the spatial scale. However, only for spatial scales $L > 40$ km, the temporal scaling exponent decreases with increasing spatial scale as found in satellite and buoy data (Rampal et al., 2008; Weiss & Dansereau, 2017). This length scale coincides with twice the wind forcing resolution indicating that the scaling characteristics of the sea ice model may be determined by the characteristics of the forcing wind fields rather than by the details of the rheology. The loss of temporal scaling for scales smaller than $\tau \leq 1$ day supports this hypothesis. The spatial scaling also breaks down for spatial scales $L \leq 10$ km. This scale coincides with the spatial resolution of the wind forcing (~ 15 km) (see Eulerian spatial scaling analysis, supporting information Figure S5). Our inferences are further supported by idealized model experiments with viscous-plastic sea ice models that showed a strong impact of wind forcing resolution on scaling characteristics of sea ice deformation (Hutter, 2015).

The poor temporal scaling points toward deficits in the VP model physics, especially as both spatial and temporal scaling emerge from an EB-model (Rampal et al., 2016). When a critical stress is reached in an EB-model, brittle deformation damages the ice and instantaneously reduces the ice strength locally. The damage information is kept over a certain healing time. In VP models, exceeding the critical stress leads to plastic deformation. A permanent weakening of the ice takes place only for large deformation events with diverging ice motion, which result in a lead of at least grid scale. The reduction in sea ice concentration and thickness leads to a lower ice strength in the next time step. Weaker ice invites more deformation at lower strain rates and hence, a positive feedback loop is generated. Compared to the instantaneous failure processes in the EB-rheology, this reduction is slow so that the temporal evolution of sea ice deformation is smooth and the scaling exponents are smaller. To improve this, the ice strength of a VP model could also be directly linked to plastic deformation occurring in a grid cell and by this introduce a memory of old deformation to the ice. To this end, a damage parameter in the ice strength parameterization could be introduced or the ice strength could be coupled directly to the plastic deformation of the previous time step. We further hypothesize that introducing a multicategory sea ice thickness distribution along with an appropriate ice strength parameterization (Rothrock, 1975) would intensify the feedback loop between ice strength and deformation. Because the standard ice strength parameterization in ice thickness distribution models (Rothrock, 1975) is determined to a large extent by the thin ice categories, the ice strength field is very heterogeneous and can lead to more deformation (Ungermann et al., 2017).

Why do VP models start to reproduce leads at higher resolution? We speculate that only at high resolution there is the potential of significantly reducing sea ice concentration within a grid cell by divergent sea ice motion, which is necessary to initiate the positive feedback cycle outlined in the previous paragraph. A weaker cell leads to larger velocity gradients in the surrounding cells and to plastic deformation. In this way, lines of grid cells of reduced ice strength are produced, along which the deformation rates localize.

6. Conclusion

A sea ice model using the VP rheology with a horizontal grid spacing of ~ 1 km reproduces LKFs along with many of the observed scaling properties of sea ice deformation. In contrast to previous studies with VP models (Girard et al., 2009), there is appropriate spatial scaling in our model simulations. The spatial scaling agrees in the seasonal variation and regional distribution with satellite observations. The VP model as configured in the LLC4320 simulation underestimates temporal scaling exponents and the coupling between spatial and temporal scaling when compared to the observed temporal scaling of sea ice deformation. We note, however, that in this study we have not made any attempt to obtain a more accurate temporal scaling by, for example, careful adjustment of the ice strength parameterization (e.g., Bouchat & Tremblay, 2017) or application of more realistic atmospheric forcing.

The new scaling analysis presented in this paper is based on Lagrangian sampling of Eulerian gridded data (LSE) and determines spatial and temporal scaling properties simultaneously for data on Eulerian grids while taking into account the advection of sea ice. With most recent sea ice deformation data sets and the output of most sea ice models provided on Eulerian grids, the LSE approach is a robust temporal scaling analysis method for gridded Eulerian data. The method evaluation relates the obtained spatial and temporal scaling to previous scaling results using either Lagrangian or Eulerian gridded data.

The good agreement of the spatial scaling with satellite observations suggests that the VP rheology, in spite of recent criticism (Girard et al., 2009), is still suitable at high spatial resolution to reproduce the spatial characteristics of sea ice deformation with its multifractal structure. Since subgrid scale damage is not parameterized in the VP model, the power-law scaling is limited to scales $L > 5$ km, as some grid cells are required to resolve a deformation feature. We cannot exclude that this limitation is a consequence of the low spatial resolution of the atmospheric forcing. The underestimation of scaling exponents in first-year ice could be addressed with a higher order dependence of the ice strength on sea ice thickness, which would reduce the stress propagation in these thin-ice areas. In general, the sensitivity of the scaling properties to model tuning parameters such as maximum ice strength P^* , shape of the yield curve, lead closing parameters, and similar, should be studied. The scaling properties could be implemented into a tuning mechanism as a measure to gauge realism of small-scale sea ice deformation in addition to other large-scale metrics such as ice extent, concentration or mean thickness.

The temporal scaling analysis implies that the crack formation of the VP model as configured in this study is too slow compared to observations. We hypothesize that an adaptation of the ice strength parameterization, in which previous plastic deformations—in analogy to the EB-rheology—induce a reduction in ice strength over a certain time, may improve the temporal scaling properties. Nevertheless, new metrics based on the temporal evolution of individual deformation events and features would help to specify the shortcomings of the model. Without any modification relative to LLC4320 setup, the VP rheology can be used to simulate processes where the small-scale temporal evolution of sea ice is not critical. For time-critical applications such as short-term forecasts, however, the VP rheology as configured in the LLC4320 setup appears inadequate.

Since the VP model reproduces localized deformation in space in agreement with satellite observations but not in time, a detailed comparison with the Maxwell-EB-rheology in the same modeling framework would give valuable insight into how different parameterizations impact small-scale deformation. Besides large-scale metrics, new ways of comparing simulations and observations based on statistics of sets of individual leads such as density, persistence, orientation, intersection angle, and length should be explored to directly identify the differences between different rheologies and satellite observations.

References

- Asplin, M. G., Galley, R., Barber, D. G., & Prinsenber, S. (2012). Fracture of summer perennial sea ice by ocean swell as a result of Arctic storms. *Journal of Geophysical Research: Oceans*, 117, C06025. <https://doi.org/10.1029/2011JC007221>
- Blanke, B., & Raynaud, S. (1997). Kinematics of the Pacific Equatorial Undercurrent: An Eulerian and Lagrangian approach from GCM results. *Journal of Physical Oceanography*, 27(6), 1038–1053. [https://doi.org/10.1175/1520-0485\(1997\)027<1038:KOTPEU>2.0.CO;2](https://doi.org/10.1175/1520-0485(1997)027<1038:KOTPEU>2.0.CO;2)
- Bouchat, A., & Tremblay, B. (2017). Using sea-ice deformation fields to constrain the mechanical strength parameters of geophysical sea ice. *Journal of Geophysical Research: Oceans*, 122, 5802–5825. <https://doi.org/10.1002/2017JC013020>
- Bouillon, S., & Rampal, P. (2015a). Presentation of the dynamical core of neXtSIM: A new sea ice model. *Ocean Modelling*, 91, 23–37. <https://doi.org/10.1016/j.ocemod.2015.04.005>

Acknowledgments

D.M. worked on modeling component of this study at the Jet Propulsion Laboratory (JPL), California Institute of Technology, under a contract with the National Aeronautics and Space Administration (NASA). High-end computing resources were provided by the NASA Advanced Supercomputing (NAS) Division of the Ames Research Center. The Arctic and Antarctic ice drift from Envisat is available at <http://rkwok.jpl.nasa.gov/envisat/index.html> and the derivation of the data set is funded by NASA's MEaSUREs program. We thank Jérôme Weiss for stimulating discussions.

- Bouillon, S., & Rampal, P. (2015b). On producing sea ice deformation data sets from SAR-derived sea ice motion. *The Cryosphere*, 9(2), 663–673. <https://doi.org/10.5194/tc-9-663-2015>
- Dansereau, V., Weiss, J., Saramito, P., & Lattes, P. (2016). A Maxwell elasto-brittle rheology for sea ice modelling. *The Cryosphere*, 10(3), 1339–1359. <https://doi.org/10.5194/tc-10-1339-2016>
- Dee, D. P., Uppala, S. M., Simmons, A. J., Berrisford, P., Poli, P., Kobayashi, S., et al. (2011). The ERA-Interim reanalysis: Configuration and performance of the data assimilation system. *Quarterly Journal of the Royal Meteorological Society*, 137(656), 553–597.
- European Centre for Medium-Range Weather Forecasts (2011). *ECMWF's operational model analysis*. Boulder CO: Research Data Archive at the National Center for Atmospheric Research, Computational and Information Systems Laboratory. <https://doi.org/10.5065/D6ZG6Q9F>
- Forget, G., Campin, J.-M., Heimbach, P., Hill, C. N., Ponte, R. M., & Wunsch, C. (2015). ECCO version 4: An integrated framework for non-linear inverse modeling and global ocean state estimation. *Geoscientific Model Development*, 8, 3071–3104.
- Girard, L., Bouillon, S., Weiss, J., Amitrano, D., Fichet, T., & Legat, V. (2011). A new modeling framework for sea-ice mechanics based on elasto-brittle rheology. *Annals of Glaciology*, 52(57), 123–132.
- Girard, L., Weiss, J., Molines, J. M., Barnier, B., & Bouillon, S. (2009). Evaluation of high-resolution sea ice models on the basis of statistical and scaling properties of Arctic sea ice drift and deformation. *Journal of Geophysical Research: Oceans*, 114, C08015. <https://doi.org/10.1029/2008JC005182>
- Herman, A., & Glowacki, O. (2012). Variability of sea ice deformation rates in the arctic and their relationship with basin-scale wind forcing. *The Cryosphere*, 6(6), 1553–1559. <https://doi.org/10.5194/tc-6-1553-2012>
- Hibler, W. D. (1979). A dynamic thermodynamic sea ice model. *Journal of Physical Oceanography*, 9, 815–846.
- Holloway, G., & Proshutinsky, A. (2007). Role of tides in Arctic ocean/ice climate. *Journal of Geophysical Research: Oceans*, 112, C04506. <https://doi.org/10.1029/2006JC003643>
- Hutchings, J. K., Heil, P., Steer, A., & Hibler, W. D. (2012). Subsynoptic scale spatial variability of sea ice deformation in the western Weddell Sea during early summer. *Journal of Geophysical Research: Oceans*, 117, C01002. <https://doi.org/10.1029/2011JC006961>
- Hutchings, J. K., Roberts, A., Geiger, C., & Richter-Menge, J. (2011). Spatial and temporal characterization of sea-ice deformation. *Annals of Glaciology*, 52(57), 360–368. <https://doi.org/10.3189/172756411795931769>
- Hutter, N. (2015). *Viscous-plastic sea-ice models at very high resolution* (Master's thesis). Bremen, Germany: University of Bremen, Alfred Wegener Institute, Helmholtz Centre for Polar and Marine research. <https://doi.org/10013/epic.46129>
- Jakobsson, M., Macnab, R., Mayer, L., Anderson, R., Edwards, M., Hatzky, J., et al. (2008). An improved bathymetric portrayal of the Arctic Ocean: Implications for ocean modeling and geological, geophysical and oceanographic analyses. *Geophysical Research Letters*, 35, L07602. <https://doi.org/10.1029/2008GL033520>
- Kwok, R. (2001). Deformation of the Arctic Ocean sea ice cover between November 1996 and April 1997: A qualitative survey. In J. Dempsey & H. Shen (Eds.), *IUTAM symposium on scaling laws in ice mechanics and ice dynamics, solid mechanics and its applications* (Vol. 94, pp. 315–322). Netherlands: Springer. https://doi.org/10.1007/978-94-015-9735-7_26
- Kwok, R. (2006). Contrasts in sea ice deformation and production in the Arctic seasonal and perennial ice zones. *Journal of Geophysical Research: Ocean*, 111, C11522. <https://doi.org/10.1029/2005JC003246>
- Kwok, R., Hunke, E. C., Maslowski, W., Menemenlis, D., & Zhang, J. (2008). Variability of sea ice simulations assessed with RGPS kinematics. *Journal of Geophysical Research: Oceans*, 113, C11012. <https://doi.org/10.1029/2008JC004783>
- Large, W. G., & Yeager, S. G. (2004). *Diurnal to decadal global forcing for ocean and sea-ice models: The data sets and flux climatologies* (Tech. Note TN-460+STR). Boulder, CO: NCAR.
- Large, W. G., McWilliams, J. C., & Doney, S. (1994). Oceanic vertical mixing: A review and a model with a nonlocal boundary layer parameterization. *Review Geophysics*, 32(4), 363–403.
- Lindsay, R. W., & Rothrock, D. A. (1995). Arctic sea ice leads from advanced very high resolution radiometer images. *Journal of Geophysical Research: Oceans*, 100(C3), 4533–4544. <https://doi.org/10.1029/94JC02393>
- Lindsay, R. W., & Stern, H. L. (2003). The radarsat geophysical processor system: Quality of sea ice trajectory and deformation estimates. *Journal of Atmospheric and Oceanic Technology*, 20(9), 1333–1347. [https://doi.org/10.1175/1520-0426\(2003\)020<1333:TRGPSQ>2.0.CO;2](https://doi.org/10.1175/1520-0426(2003)020<1333:TRGPSQ>2.0.CO;2)
- Lindsay, R. W., Zhang, J., & Rothrock, D. A. (2003). Sea-ice deformation rates from satellite measurements and in a model. *Atmosphere-Ocean*, 41(1), 35–47. <https://doi.org/10.3137/ao.410103>
- Losch, M., Fuchs, A., Lemieux, J.-F., & Vanselow, A. (2014). A parallel Jacobian-free Newton-Krylov solver for a coupled sea ice-ocean model. *Journal of Computational Physics*, 257(Part A), 901–911. <https://doi.org/10.1016/j.jcp.2013.09.026>
- Losch, M., Menemenlis, D., Campin, J.-M., Heimbach, P., & Hill, C. (2010). On the formulation of sea-ice models. Part 1: Effects of different solver implementations and parameterizations. *Ocean Modelling*, 33, 129–144. <https://doi.org/10.1016/j.ocemod.2009.12.008>
- Marko, J. R., & Thomson, R. E. (1977). Rectilinear leads and internal motions in the ice pack of the Western Arctic Ocean. *Journal of Geophysical Research*, 82(6), 979–987. <https://doi.org/10.1029/JC082i006p00979>
- Marsan, D., Stern, H., Lindsay, R., & Weiss, J. (2004). Scale dependence and localization of the deformation of Arctic sea ice. *Physical Review Letters*, 93, 178501. <https://doi.org/10.1103/PhysRevLett.93.178501>
- Marsan, D., & Weiss, J. (2010). Space/time coupling in brittle deformation at geophysical scales. *Earth and Planetary Science Letters*, 296(3/4), 353–359. <https://doi.org/10.1016/j.epsl.2010.05.019>
- Marshall, J., Adcroft, A., Hill, C., Perelman, L., & Heisey, C. (1997). A finite-volume, incompressible Navier Stokes model for studies of the ocean on parallel computers. *Journal of Geophysical Research: Oceans*, 102(C3), 5753–5766. <https://doi.org/10.1029/96JC02775>
- Menemenlis, D., Campin, J., Heimbach, P., Hill, C., Lee, T., Nguyen, A., et al. (2008). ECCO2: High resolution global ocean and sea ice data synthesis. *Mercator Ocean Quarterly Newsletter*, 31, 13–21.
- MITgcm Group (2017). *MITgcm user manual, online documentation*. Cambridge, MA: MIT/EAPS. Retrieved from http://mitgcm.org/public/r2_manual/latest/online_documents
- Nguyen, A. T., Menemenlis, D., & Kwok, R. (2009). Improved modeling of the Arctic halocline with a subgrid-scale brine rejection parameterization. *Journal of Geophysical Research: Oceans*, 114, C11014. <https://doi.org/10.1029/2008JC005121>
- Nguyen, A. T., Menemenlis, D., & Kwok, R. (2011). Arctic ice-ocean simulation with optimized model parameters: Approach and assessment. *Journal of Geophysical Research: Oceans*, 116, C04025. <https://doi.org/10.1029/2010JC006573>
- Oikkonen, A., Haapala, J., Lensu, M., Karvonen, J., & Itkin, P. (2017). Small-scale sea ice deformation during N-ICE2015: From compact pack ice to marginal ice zone. *Journal of Geophysical Research: Oceans*, 122, 5105–5120. <https://doi.org/10.1002/2016JC012387>
- Ponte, R. M., Chaudhuri, A. H., & Vinogradov, S. V. (2015). Long-period tides in an atmospherically driven, stratified ocean. *Journal of Physical Oceanography*, 45(7), 1917–1928.
- Rampal, P., Bouillon, S., Ólason, E., & Morlighem, M. (2016). neXtSIM: A new Lagrangian sea ice model. *The Cryosphere*, 10(3), 1055–1073. <https://doi.org/10.5194/tc-10-1055-2016>

- Rampal, P., Weiss, J., Marsan, D., Lindsay, R., & Stern, H. (2008). Scaling properties of sea ice deformation from buoy dispersion analysis. *Journal of Geophysical Research: Oceans*, 113, C03002. <https://doi.org/10.1029/2007JC004143>
- Richter-Menge, J. A., McNutt, S. L., Overland, J. E., & Kwok, R. (2002). Relating Arctic pack ice stress and deformation under winter conditions. *Journal of Geophysical Research: Oceans*, 107(C10), 8040. <https://doi.org/10.1029/2000JC000477>
- Rocha, C. B., Chereskin, T. K., Gille, S. T., & Menemenlis, D. (2016a). Mesoscale to submesoscale wavenumber spectra in Drake Passage. *Journal of Physical Oceanography*, 46(2), 601–620. <https://doi.org/10.1175/JPO-D-15-0087.1>
- Rocha, C. B., Gille, S. T., Chereskin, T. K., & Menemenlis, D. (2016b). Seasonality of submesoscale dynamics in the Kuroshio Extension. *Geophysical Research Letters*, 43(21), 11304–11311. <https://doi.org/10.1002/2016GL071349>
- Rothrock, D. A. (1975). The energetics of the plastic deformation of pack ice by ridging. *Journal of Geophysical Research*, 80(33), 4514–4519. <https://doi.org/10.1029/JC080i033p04514>
- Rothrock, D. A., & Thorndike, A. S. (1984). Measuring the sea ice floe size distribution. *Journal of Geophysical Research: Oceans*, 89(C4), 6477–6486. <https://doi.org/10.1029/JC089iC04p06477>
- Spren, G., Kwok, R., Menemenlis, D., & Nguyen, A. T. (2016). Sea ice deformation in a coupled ocean-sea ice model and in satellite remote sensing data. *The Cryosphere Discussions*, 2016, 1–37. <https://doi.org/10.5194/tc-2016-13>
- Squire, V. A., Dugan, J. P., Wadhams, P., Rottier, P. J., & Liu, A. K. (1995). Of ocean waves and sea ice. *Annual Review of Fluid Mechanics*, 27(1), 115–168. <https://doi.org/10.1146/annurev.fl.27.010195.000555>
- Stern, H. L., & Lindsay, R. W. (2009). Spatial scaling of arctic sea ice deformation. *Journal of Geophysical Research: Oceans*, 114, C10017. <https://doi.org/10.1029/2009JC005380>
- Ungermann, M., Tremblay, L. B., Martin, T., & Losch, M. (2017). Impact of the ice strength formulation on the performance of a sea ice thickness distribution model in the arctic. *Journal of Geophysical Research: Oceans*, 122, 2090–2107. <https://doi.org/10.1002/2016JC012128>
- Wang, Q., Danilov, S., Jung, T., Kaleschke, L., & Wernecke, A. (2016). Sea ice leads in the Arctic Ocean: Model assessment, interannual variability and trends. *Geophysical Research Letters*, 43, 7019–7027. <https://doi.org/10.1002/2016GL068696>
- Weiss, J. (2003). Scaling of fracture and faulting of ice on earth. *Surveys in Geophysics*, 24(2), 185–227. <https://doi.org/10.1023/A:1023293117309>
- Weiss, J. (2017). Exploring the solid turbulence of sea ice dynamics down to unprecedented small scales. *Journal of Geophysical Research: Oceans*, 122, 6071–6075. <https://doi.org/10.1002/2017JC013236>
- Weiss, J., & Dansereau, V. (2017). Linking scales in sea ice mechanics. *Philosophical Transactions of the Royal Society of London A: Mathematical, Physical and Engineering Sciences*, 375, 20150352. <https://doi.org/10.1098/rsta.2015.0352>